Contents lists available at ScienceDirect

Nuclear Instruments and Methods in Physics Research A

Assessment of neural networks training strategies for histomorphometric analysis of synchrotron radiation medical images ☆

Anderson Alvarenga de Moura Meneses [a,b,*], Christiano Jorge Gomes Pinheiro [c], Paola Rancoita [b,d], Tom Schaul [b], Luca Maria Gambardella [b], Roberto Schirru [a], Regina Cely Barroso [c], Luís Fernando de Oliveira [c]

[a] Federal University of Rio de Janeiro, COPPE, Nuclear Engineering Program, CP 68509, CEP 21.941-972, Rio de Janeiro, RJ, Brazil
[b] IDSIA (Dalle Molle Institute for Artificial Intelligence), University of Lugano, Switzerland
[c] State University of Rio de Janeiro, RJ, Brazil
[d] Mathematics Department, Università degli Studi di Milano, Italy

ARTICLE INFO

ABSTRACT

Micro-computed tomography (μCT) obtained by synchrotron radiation (SR) enables magnified images with a high space resolution that might be used as a non-invasive and non-destructive technique for the quantitative analysis of medical images, in particular the histomorphometry (HMM) of bony mass. In the preprocessing of such images, conventional operations such as binarization and morphological filtering are used before calculating the stereological parameters related, for example, to the trabecular bone microarchitecture. However, there is no standardization of methods for HMM based on μCT images, especially the ones obtained with SR X-ray. Notwithstanding the several uses of artificial neural networks (ANNs) in medical imaging, their application to the HMM of SR-μCT medical images is still incipient, despite the potential of both techniques. The contribution of this paper is the assessment and comparison of well-known training algorithms as well as the proposal of training strategies (combinations of training algorithms, sub-image kernel and symmetry information) for feed-forward ANNs in the task of bone pixels recognition in SR-μCT medical images. For a quantitative comparison, the results of a cross validation and a statistical analysis of the results for 36 training strategies are presented. The ANNs demonstrated both very low mean square errors in the validation, and good quality segmentation of the image of interest for application to HMM in SR-μCT medical images.

1. Introduction

The synchrotron radiation (SR) [1] is obtained from high-velocity charged particles that move into magnetic fields, and may be produced in different wavelengths of the electromagnetic spectrum, for example, X-rays [2,3]. Nowadays, third generation SR facilities have increased the utilization of SR X-ray imaging in many scientific areas. SR sources have revolutionized many existing techniques as a basis for novel experimental approaches as well. SR sources offer a much higher brilliance compared to X-ray tubes and very high flux at small source size, at least a thousand times larger, such that the investigation of samples at the micro- and even sub-micrometer level becomes feasible. For

medical purposes, the SR X-rays might be used in the micro-computed tomography (μCT) [4] for several applications. One application is the non-invasive and non-destructive quantitative analysis of biological tissues for studies related to diseases such as cancer and osteoporosis.

In the case of the osteoporosis, a disease whose spread has impacts on both economy and society [5], both bone mass quantification and histomorphometry (HMM [6], the quantitative measurement parameters for the structural characterization) of bony tissue are critically important. For example, with histomorphometric analyses of medical images, it is possible to assess the structure of trabecular bone, which can provide important information for diagnosis and treatment [7].

High resolution techniques might be great allies of the HMM: Chappard et al. [8] review the technologies and parameters used to measure trabecular bone microarchitecture. Nevertheless, according to the authors, "μCT is only at its beginning and there is yet no standardization of parameters between manufacturers". However, the development of new imaging techniques with high

definition, such as SR-µCT, plays an important role for the progress of diagnosis based on medical imaging.

Simple examples where the usage of medical imaging-based diagnosis might be particularly important in comparison to the diagnosis based on biopsies are in Refs. [9–11]. In Refs. [9,10] the bone biopsies were obtained during surgeries. In Ref. [11], a study on periodontal HMM was performed in sheep, requiring the sacrifice of the animals. In fact, standardized analysis methods for high resolution three-dimensional medical images, that are equivalent to classical methods, would have the enormous advantage of reducing the necessity of surgeries and animal sacrifice. In addition, it might indirectly lead to a greater number of assessments and studies as well.

Moreover, Schouten et al. [12] indicate drawbacks of histological sectioning such as the time consumed, the prevention of the specimen for being used for other experiments and loss of material, asserting that "however, as µCT is still relatively new, the procedures utilized to assess and analyze bone structure quantitatively are not yet fully standardized".

Still in Ref. [12], the assessment and comparison among conventional and µCT-based HMM is performed with a different threshold for each image based on their histogram, selected to preserve the bone tissue in the images, which, according to the authors, might have the drawback of variability among observers. The authors remark that the measurement with the µCT images is not reliable with respect to conventional HMM despite the important three-dimensional information provided by µCT images. Unfortunately, the use of threshold-dependent techniques for medical imaging has this sort of disadvantage.

Thus, to progress in computational methods for the application to SR X-ray µCT images for HMM might be an important step towards advances in treatment and diagnosis of diseases such as osteoporosis. In this article, we survey the application of neural computing to high-resolution SR medical images for HMM. Neural computing represents a consolidated branch of artificial intelligence (AI) with successful applications of the artificial neural networks (ANNs) [13] in several fields, used in classification, pattern recognition and regression. The usage of ANNs is interesting due to its attractive characteristics for pattern recognition and classification and contrasting with the conventional techniques that impose a threshold during the analysis.

In this case, bone pixel classification for the segmentation focused on HMM requires an accuracy and precision which might be provided by the high quality of the SR X-ray µCT images. Those accuracy issues are not commonly investigated in applications such as the segmentation in medical images for visualization of organs or physiological behavior, and therefore a survey of the application of ANNs for this task in this context is proposed in this article.

A recent investigation [14] demonstrated that feed forward (FF) ANNs are suitable for the recognition of bone pixels in raw SR X-ray µCT medical image slices, that is, without any sort of preprocessing such as normalization, filters or binarization. In fact, to the best of our knowledge, there are very few papers describing AI techniques applied to SR medical images for HMM. Therefore, as a first step towards the application of AI techniques for HMM in SR X-ray µCT images, we here present a study comprising the statistical analysis and assessment of different architectures, training algorithms and symmetry strategies of FF-ANNs with the back-propagation [15] training algorithm.

In this article, our main concern is the assessment of *training strategies* for FF-ANNs in the bone pixel classification in SR medical images for HMM. Training strategies represent the combination of training algorithms with kernels (dimensions of the training subimages, such as 3×3, or 5×5, or 7×7 pixels) and a type of symmetry. The latter are alternative ways of presenting

Fig. 1. The image of interest: a slice of a rodent's tibia cortical bone obtained with synchrotron radiation X-Ray µCT at the ELETTRA Laboratory, at Trieste.

input information to the ANN, such as raw grayscale values, averages of different groups of pixels related to their orientation symmetry in relation to the central pixel, or averages of different groups of pixels that surround the central pixel (for details, see Section 3). It is well-known that different training algorithms have different performance on the same problem, which leads to the necessity of their comparison. Going one step further, we compare results not only for training algorithms, but also for full training strategies. The assessment of the classification performance of ANNs trained using those training strategies was based on the leave one out cross validation (LOOCV) methodology [16].

The image used for the experiments is depicted in Fig. 1. It represents a slice of a rodent's tibia cortical bone obtained with SR X-ray µCT at the synchrotron radiation for medical physics (SYRMEP) beam line of the ELETTRA Laboratory at Trieste, Italy (www.elettra.trieste.it). The darker grayscale pixels are background, and the intermediate grayscale pixels region is marrow. The region of interest is the lighter one, which is bone.

The remaining of this article is organized as follows: Section 2 presents the aspects of the SR-µCT medical imaging and the HMM, as well as details about the instrumentation; Section 3 focuses on the ANNs and the training strategies applied to the SR-µCT medical images for HMM; the methodology is described in Section 4; Section 5 presents the experimental results; we discuss them in Section 6 before concluding in Section 7.

2. Synchrotron radiation medical imaging for histomorphometric analysis

2.1. Synchrotron radiation medical imaging at ELETTRA laboratory

SR facilities such as the ELETTRA Laboratory (Trieste, Italy) provide important characteristics for the acquisition of medical images. The image of interest was obtained at the synchrotron radiation for medical physics (SYRMEP) beam line, which is designed for *in-vitro* samples X-Ray imaging. The beam is laminar and extremely collimated. The SR beams are, to a good extent, coherent, allowing higher sensitivity and better spatial resolution and this is an important factor for innovative imaging techniques. Moreover, the high brilliance of the synchrotron light allows the use of monochromatic radiation, i.e., the selection of single photon energy. Monochromaticity avoids beam hardening and

therefore turns a reconstructed radiography in a quantitative mapping of X-ray attenuations.

Despite the enhancement of biological tissue imaging due to the monochromaticity and coherence of SR beams, radiological imaging based only on absorption effects results in poor image contrast [17]. Notwithstanding, the information carried by the phase of X-Ray wavefield, or *phase effects*, may be exploited by techniques that convert it into image contrast, enhancing detail visibility [18].

Lewis [19] reviewed the three experimental techniques used in order to obtain images with contrast enhancement based on phase-shift effects: X-Ray interferometry, diffraction enhanced imaging and in-line holography (also called free-space propagation or merely *phase contrast* imaging [18]).

In phase contrast imaging, waves are refracted by details, interfering with unrefracted waves, resulting in strong interference patterns that are detected [17], enhancing the contrast of the detail borders, for example. The effect of the phase contrast may be noticed in the image of interest (Fig. 1): the borders of bony tissue and marrow became lighter.

Phase contrast imaging is one such technique that exploits differences in the real part of the refractive index distribution of an object to form an image using a spatially coherent light source. It may permit the visualization of objects that have very similar X-ray absorption properties, and therefore is particularly useful for biological tissue imaging in medical applications. In addition, microtomographic processing techniques can be applied readily to phase contrast images [20].

2.2. Micro-computed tomography (μCT)

The μCT is an emerging technique for the non-destructive assessment and analysis of the 3D trabecular bone structure. The basis of tomography is X-ray radiography. According to the equation that governs the image intensity in projection imaging, an X-ray beam is sent through a sample and the transmitted beam is recorded on a charge-coupled device (CCD). The Beer–Lambert law (Eq. (1)) is the linear relationship between absorbance and concentration of an absorbing species. The ratio of transmitted intensity $I(x)$ to incident intensity $I_0(x)$ is related to the line integral of the absorption coefficient of the material $\mu(x, y)$ along the path L that the photons follow through the sample:

$$I(x) = I_0(x)\exp\left(-\int_L \mu(x,y)dy\right). \tag{1}$$

The SR-μCT is a very useful technique when it comes to three-dimensional imaging of many geometries. The SR properties enable SR-μCT to reconstruct the highly resolved 3D image even with a high signal-to-noise ratio [21].

2.3. Histomorphometric analysis

Histomorphometric analysis has been used to evaluate different complex structures such as ceramic filters, net structures and cancellous objects (e.g. bone), which have inner connected structures. In the last years, histomorphometric analysis has been studied to quantify cortical bone or vascular canal network structure. The three-dimensional HMM, obtained from μCT, corresponds to an evolution of the conventional method that is based on 2D analysis [22,23]. The measured parameters are sample volume (BV), sample surface (BS), ratio of sample volume to total volume (BV/TV), ratio of surface to volume of the sample (BS/BV), connection thickness (Tb$_{Th}$), connection number (Tb$_N$) and connection separation (Tb$_{Sp}$). These first five parameters form the base of histomorphometric analysis [24,25] and some

parameters like BV, BS and TV may be transferable to the analysis of the cortical bone.

The 3D reconstructed data are a collection of coefficients distributed regularly in space. Each set of eight coefficients (seen as pixels), displaced as a cube, forms a voxel. Once the 3D map of the bone specimens is achieved using μCT, the specimen is fragmented into voxels, each one representing a single solid, following the same procedure established to compute the 3D histomorphometric parameters. For conventional techniques and the Feldkamp procedure [6], all parameters are evaluated from slices. The 3D HMM is more compatible with the morphologic parameters volume and surface. The obtained results reveal the potential in using 3D tomography to extract and evaluate histomorphometric parameters, compared to 2D analysis, since it avoids extrapolations.

The 3D tomography yields all the spatial information needed to evaluate the parameters BV/TV and BS/BV directly from the volume. The total volume (TV) is the number of voxels contained on the volume data file. The total surface and the volume of the microstructure are computed by summing the areas and volumes of each individual model found in the data volume.

2.4. Instrumentation

All specimens were imaged using SR μCT at SYRMEP beam line, on the ELETTRA SR facility. The beam line provides a monochromatic laminar-section X-ray with a maximum area of about 160×5 mm^2 at 20 keV, at a distance of about 23 m from the source. The system consists of a Si (1 1 1) crystal working at Bragg configuration. The useful energy range is 8–35 keV. The intrinsic energy resolution of the monochromator is about 10^{-3}. Typical flux measured at the sample position at 17 keV is about 1.6×10^8 photons/mm^2 s with a stored electron beam of 300 mA as ELETTRA operates at 2 GeV [17]. A custom-built ionization chamber is placed upstream to the sample to determine the exposure on the sample. A micrometric vertical and horizontal translation stage allows the positioning and the scanning of the sample with respect to the stationary beam and a rotational stage allows CT acquisition with a resolution of 0.001°.

The detector system is comprised of a 16-bit CCD camera, with 2048×2048 pixels^2, 14×14 μm^2 pixel size, coupled to an intensifier screen with no magnification (1:1). The CCD camera can move along the sample-detector axis, in order to set the desired sample-to-detector distance d. According to the choice of the sample-to-detector distance, one may distinguish between the absorption and phase sensitive regimes. If the CCD is mounted very close to the sample we are in the absorption regime. For higher d values, free space propagation transforms the phase modulation of the transmitted beam into an amplitude modulation.

3. Training strategies for artificial neural networks in synchrotron radiation medical imaging

3.1. Artificial neural networks and their application to synchrotron radiation medical imaging

Neural computing is part of the field of computational intelligence. It studies and develops models inspired by the brain, seen as a "highly complex, non-linear and parallel" computer [13]. ANNs are models based upon the relationships among neurons, synapses and learning, and are used for tasks such as regression and classification.

Egmont-Petersen et al. [26] review the solutions involving ANNs in image processing and analysis. In order to systematically cover and comprehensibly explain the role of ANNs in image processing, the authors adopt a taxonomy for image processing tasks that comprises preprocessing, data reduction, segmentation, object recognition, image understanding and optimization. The work depicted herein aims to assess the performance of bone pixel classification provided by ANNs, for application to the segmentation of SR X-ray μCT images. Although some of the works cited in [26] are on FF-ANNs applied to medical images, none of them is related to SR images and their specificities. Neither do they report precision or accuracy of classification performed by ANNs focused on quantitative analysis for medical imaging (HMM in particular), which operates under a different set of goals and requirements than for example segmentation for visualization.

In Ref. [14], bone pixel recognition by FF-ANNs in SR X-ray μCT medical images was demonstrated with an assessment performed with the receiver operating characteristic curves methodology. In order to accomplish the pattern recognition task, the FF-ANNs in Ref. [14] had 9 neurons in the input layer, 5 neurons in the hidden layer and 3 neurons in the output layer. They were trained with 30 vectors corresponding to 30 patterns (subimages), 10 for each phase (bone, background and marrow). Each vector was composed by 9 (nine) grayscale values of the pixels, and during the training, the neurons of the input layer received these real values between 0 (black) and 1 (white), corresponding to the grayscale value of each pixel. Since the training was supervised, for each input pattern, an output vector was associated: (1 0 0) for background, (0 1 0) for bone and (0 0 1) for marrow. Besides, three different types of supervised learning algorithms were tested: gradient descent, gradient descent with momentum and gradient descent with variable learning rate. The results in Ref. [14] demonstrated the viability of application of FF-ANNs to bone

pixel recognition in SR X-ray medical images, although an assessment of the accuracy was not included. The promising results sparked an interest in examining a broader range of different training strategies, which will be discussed in the next subsection.

3.2. Training strategies

In the present survey we have used FF-ANNs with more complex training algorithms than in Ref. [14]: gradient descent with adaptive learning rate and momentum training (GDLRM), resilient backpropagation (RB), the quasi-Newton BFGS and Levenberg–Marquardt (LM) [27].

The combination of those training algorithms with different kernels and symmetry information yielded what we call training strategies. We were interested in presenting as input to the ANNs kernels ("masks" for the subimages) of different dimensions and symmetry information aiming to convey context information based on the pixels' intensity. We have tested the dimensions 3×3, or 5×5 and 7×7 pixels for the kernels in the training strategies.
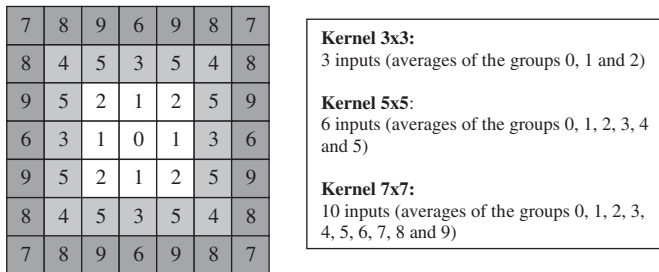

Fig. 2. Symmetry information *SymAv*1 for the subimages used to train the ANNs (average intensity of groups of grayscale pixels, related to the orientation): 3 inputs for a 3×3 kernel—white pixels; 6 inputs for a 5×5 kernel—white and light gray pixels; and 10 inputs for a 7×7 kernel—white, light gray and dark gray pixels.
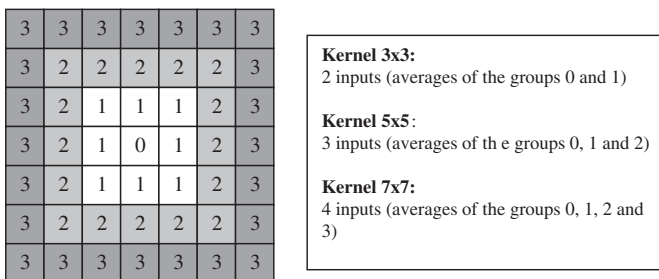
Fig. 3. Symmetry information *SymAv*2 for the subimages used to train the ANNs (average intensity of groups of grayscale pixels, surrounding the central pixel): 2 inputs for a 3×3 kernel—white pixels; 3 inputs for a 5×5 kernel—white and light gray pixels; and 4 inputs for a 7×7 kernel—white, light gray and dark gray pixels.

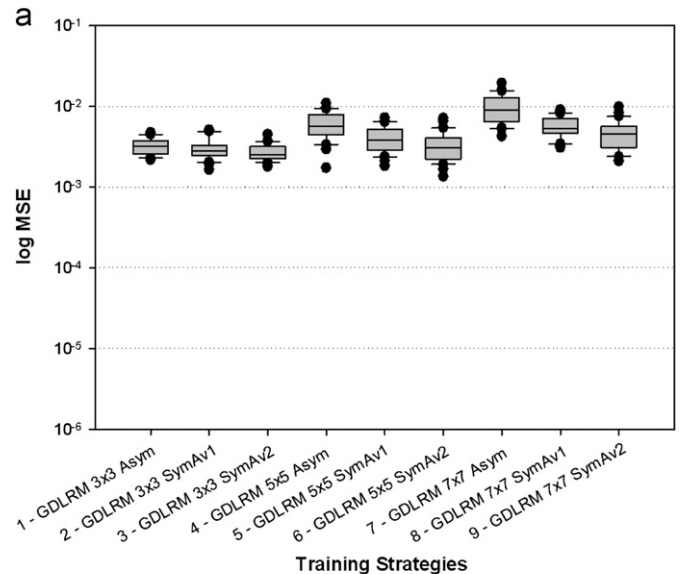**Fig. 4.** (a) Box plots of the MSEs (log) for different training strategies with the algorithm GDLRM. (b) As an example, the image of Fig. 1 segmented with the classification provided by the ANN trained with the strategy GDLRM 3×3 *SymAv*2.

Our approach is different from both Ref. [28] and Ref. [29], which uses a symmetric architecture in order to perform rotation-invariant pattern recognition, or reduce redundant weights of the ANN using a symmetrical architecture or by imposing equal weights. In the assessment of training strategies we compared ways of conveying symmetry information, which we call *Asym*, *SymAv*1 and *SymAv*2. In the conventional asymmetric approach (*Asym*), the numbers of inputs of the pixel's grayscale values were: 9 inputs for a 3×3 kernel, 25 inputs for a 5×5 kernel and 49 inputs for a 7×7 kernel. On the other hand, in the symmetric approach (*SymAv*1 and *SymAv*2), the average of intensity (grayscale values) of different groups of pixels was used, as depicted in Figs. 2 and 3. In the case of the average value for groups related to the orientation (*SymAv*1), Fig. 2 exhibits 3 inputs for a 3×3 kernel (instead of 9 inputs), 6 inputs for a 5×5 kernel (instead of 25 inputs) and 10 inputs for a 7×7 kernel (instead of 49 inputs); for average values of groups surrounding the central pixel (*SymAv*2), Fig. 3 exhibits 2 inputs for a 3×3 kernel (instead of 9 inputs), 3 inputs for a 5×5 kernel (instead of 25 inputs) and 4 inputs for a 7×7 kernel (instead of 49 inputs). The main idea with this approach is the following: with a smaller number of inputs,

there are fewer weights to be adjusted in the ANN, reducing redundancy and thereby making ANN learning both more efficient and less prone to overfitting.

In short, each training algorithm (*GDLRM*, *RB*, *BFGS* and *LM*) was combined with a type of kernel (3×3, 5×5 or 7×7) and one type of symmetry assumption (*Asym*, *SymAv*1 or *SymAv*2), resulting in 9 combinations for each training algorithm, that is, 36 training strategies.

4. Methodology

A *classifier* is a function which is able to map from unlabeled instances to class labels. It is induced by an algorithm that builds it from a data set [16]. In our case, the ANNs are the classifiers, and supervised learning (with the specificities of each training strategy as stated before) plays the role of the induction algorithm and the instances are the pixels to be classified. A description of the supervised learning methodology for ANNs is given in Ref. [13].

Some methods such as bootstrap, holdout or LOOCV may be used to estimate the future prediction accuracy of a classifier [16].

Fig. 5. (a) Box plots of the MSEs (log) for different training strategies with the algorithm RB. (b) The image of Fig. 1 segmented with the classification provided by the ANN trained with the strategy RB 3×3 *SymAv*2.
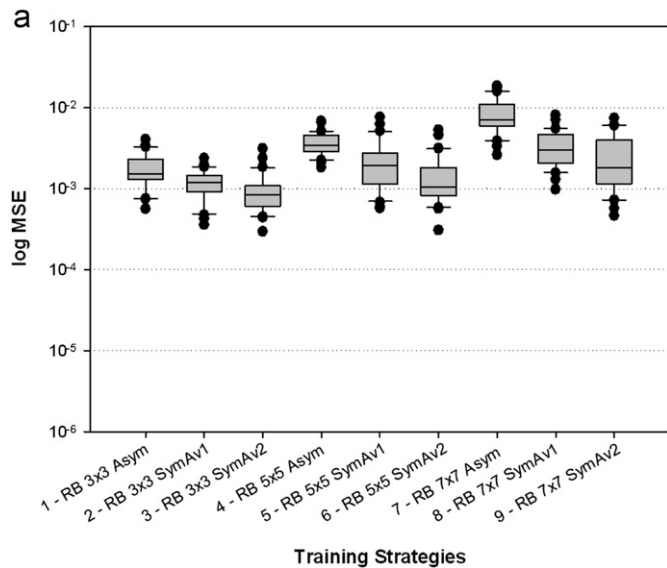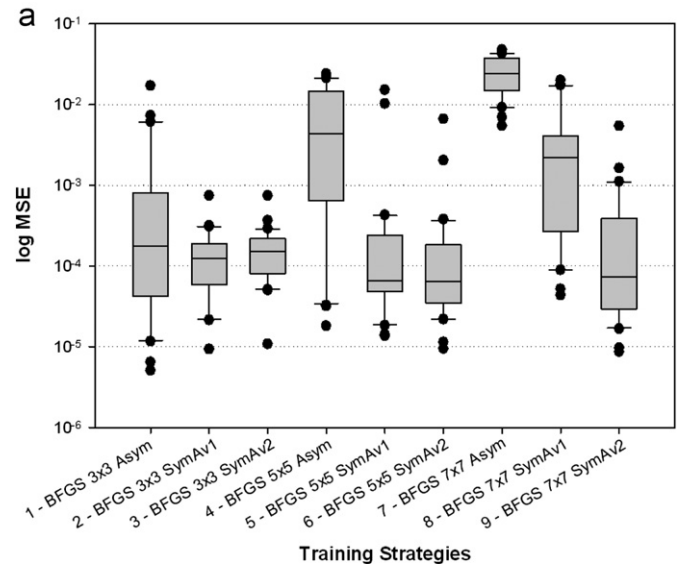

Fig. 6. (a) Box plots of the MSEs (log) for different training strategies with the algorithm BFGS. (b) The image of Fig. 1 segmented with the classification provided by the ANN trained with the strategy BFGS 3×3 *SymAv*1.

In our work we used the LOOCV and the mean square errors provided by the LOOCV. The main idea with the LOOCV is that the classifier will be initialized and trained k times by the induction algorithm. Given a set S with k instances $S = \{X_1, X_2, \ldots, X_k\}$ and their respective classification, for each test t_i in $T = \{t_1, t_2, \ldots, t_k\}$, the classifier is trained with $k-1$ instances, since during the test t_i, the instance X_i is *left out* from the training phase in t_i, and X_i will be submitted to classification and therefore an estimation of misclassification of X_i can be calculated. In other words, the classifier is always trained with a subset of instances and tested with the instance that was not used in the training phase. Thus, it is possible to estimate the accuracy of classifiers based on the classification of an instance that was not presented during the training phase in order to compare, choose, combine or estimate the bias and variance of future processes of classification.

Our ANNs had one hidden layer with 5 neurons, and only one output for the classification (0 for no-bone, or 1 for bone). The number of neurons in the input layer depended on the training strategy, as mentioned in Section 3.2 (*Asym*: 9, 25 or 49 inputs; *SymAv*1: 3, 6 or 10 inputs; *SymAv*2: 2, 3 or 4 inputs).

In this work, 50 pixels of interest from Fig. 1 were selected and classified in order to compose the set S (25 bone pixels, 13

marrow pixels and 12 background pixels). The same set S was used for all training strategies, for all ANNs tested. During the training phases, the stopping criterion was either 4000 epochs or an MSE of the training phase lower than 10^{-5}. The pixel intensity information corresponding to the 49 instances, according to the information symmetries depicted in Figs. 2 and 3, was presented to the ANN as well as their classification during the training phase with a given training strategy. Then, the trained ANN was used for the classification of the *left-out* pixel, yielding, for the test t_i a square error SE_i of the output provided by the ANN in relation to the pixel's classification (0 for no-bone, or 1 for bone). For the test t_{i+1}, the ANN is re-initialized randomly and the process is started over again. Then, the MSE over the 50 SEs was calculated. This procedure (MSE for the LOOCV of the 50 pixels of the set S) was repeated 30 times for each training strategy, yielding 30 MSEs, and the box plots were plotted with the log of the MSEs for a better visualization.

In short, each LOOCV yielded one MSE and we repeated 30 times the LOOCV for each training strategy. The comparison between the results is useful to determine which training strategies are likely to have a good accuracy in bone pixel classification for SR X-ray μCT images for HMM.
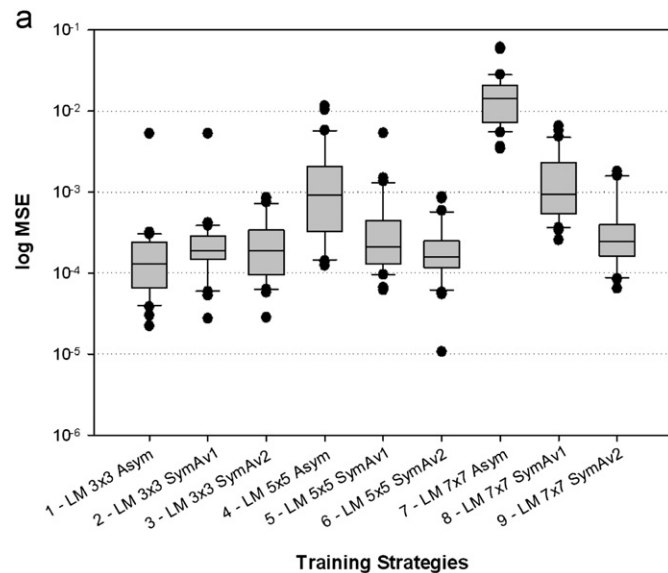
5. Computational experimental results

The box plots of the log MSEs for the LOOCVs of the ANNs trained with the algorithms GDLRM, RB, BFGS and LM are depicted in Figs. 4a–7a. Images obtained by segmentation performed by ANNs (trained with training strategies chosen after the analysis) are presented in Figs. 4b–7b. They are illustrative examples of the final results of the segmentation of Fig. 1. Although they look very similar, slight differences may be noticed.

Tables 1–4 exhibit the average MSE for each training strategy, as well as its standard deviation and confidence interval of the mean at level 95%. Fig. 8 depicts the box plots of the best training

Fig. 7. (a) Box plots of the MSEs (log) for different training strategies with the algorithm LM. (b) The image of Fig. 1 segmented with the classification provided by the ANN trained with the strategy LM 3×3 *Asym*.

Table 1
Average MSEs, standard deviations and t-Intervals for different training strategies for the training algorithm GDLRM.

	Av. MSE	St. dev.	t-Int1	t-Int2
GDLRM 3×3 *Asym*	3.20×10^{-3}	7.25×10^{-4}	2.93×10^{-3}	3.47×10^{-3}
GDLRM 3×3 *SymAv*1	2.98×10^{-3}	8.77×10^{-4}	2.66×10^{-3}	3.31×10^{-3}
GDLRM 3×3 *SymAv*2	2.69×10^{-3}	6.23×10^{-4}	2.46×10^{-3}	2.92×10^{-3}
GDLRM 5×5 *Asym*	6.10×10^{-3}	2.24×10^{-3}	5.26×10^{-3}	6.93×10^{-3}
GDLRM 5×5 *SymAv*1	4.06×10^{-3}	1.49×10^{-3}	3.50×10^{-3}	4.62×10^{-3}
GDLRM 5×5 *SymAv*2	3.33×10^{-3}	1.38×10^{-3}	2.82×10^{-3}	3.85×10^{-3}
GDLRM 7×7 *Asym*	9.79×10^{-3}	3.83×10^{-3}	8.36×10^{-3}	1.12×10^{-2}
GDLRM 7×7 *SymAv*1	5.74×10^{-3}	1.75×10^{-3}	5.08×10^{-3}	6.39×10^{-3}
GDLRM 7×7 *SymAv*2	4.59×10^{-3}	1.38×10^{-3}	2.82×10^{-3}	3.85×10^{-3}

Table 2
Average MSEs, standard deviations and t-Intervals for different training strategies for the training algorithm RB.

	Av. MSE	St. dev.	t-Int1	t-Int2
RB 3×3 *Asym*	1.78×10^{-3}	8.42×10^{-4}	1.46×10^{-3}	2.09×10^{-3}
RB 3×3 *SymAv*1	1.21×10^{-3}	4.68×10^{-4}	1.04×10^{-3}	1.39×10^{-3}
RB 3×3 *SymAv*2	9.82×10^{-4}	5.99×10^{-4}	7.59×10^{-4}	1.21×10^{-3}
RB 5×5 *Asym*	3.69×10^{-3}	1.21×10^{-3}	3.23×10^{-3}	4.14×10^{-3}
RB 5×5 *SymAv*1	2.33×10^{-3}	1.70×10^{-3}	1.70×10^{-3}	2.97×10^{-3}
RB 5×5 *SymAv*2	1.49×10^{-3}	1.15×10^{-3}	1.06×10^{-3}	1.92×10^{-3}
RB 7×7 *Asym*	8.59×10^{-3}	4.22×10^{-3}	7.02×10^{-3}	1.02×10^{-2}
RB 7×7 *SymAv*1	3.47×10^{-3}	1.71×10^{-3}	2.83×10^{-3}	4.11×10^{-3}
RB 7×7 *SymAv*2	2.66×10^{-3}	1.89×10^{-3}	1.95×10^{-3}	3.36×10^{-3}

Table 3
Average MSEs, standard deviations and t-Intervals for different training strategies for the training algorithm BFGS.

	Av. MSE	St. dev.	t-Int1	t-Int2
BFGS 3×3 Asym	1.61×10^{-3}	3.56×10^{-3}	2.75×10^{-4}	2.94×10^{-3}
BFGS 3×3 SymAv1	1.52×10^{-4}	1.41×10^{-4}	9.90×10^{-5}	2.04×10^{-4}
BFGS 3×3 SymAv2	1.72×10^{-4}	1.36×10^{-4}	1.21×10^{-4}	2.23×10^{-4}
BFGS 5×5 Asym	7.73×10^{-3}	8.14×10^{-3}	4.69×10^{-3}	1.08×10^{-2}
BFGS 5×5 SymAv1	9.54×10^{-4}	3.25×10^{-3}	0	2.17×10^{-3}
BFGS 5×5 SymAv2	3.77×10^{-4}	1.23×10^{-3}	0	8.37×10^{-4}
BFGS 7×7 Asym	2.56×10^{-2}	1.26×10^{-2}	2.09×10^{-2}	3.03×10^{-2}
BFGS 7×7 SymAv1	4.22×10^{-3}	6.00×10^{-3}	1.98×10^{-3}	6.46×10^{-3}
BFGS 7×7 SymAv2	4.36×10^{-4}	1.02×10^{-3}	5.47×10^{-5}	8.16×10^{-4}

Table 4
Average MSEs, standard deviations and t-Intervals for different combinations of Kernel/Strategy for the training algorithm LM.

|	Av. MSE	St. dev.	t-Int1	t-Int2
LM 3×3 Asym	3.17×10^{-4}	9.37×10^{-4}	0	6.67×10^{-4}
LM 3×3 SymAv1	3.72×10^{-4}	9.29×10^{-4}	2.45×10^{-5}	7.19×10^{-4}
LM 3×3 SymAv2	2.56×10^{-4}	2.22×10^{-4}	1.73×10^{-4}	3.39×10^{-4}
LM 5×5 Asym	2.06×10^{-3}	2.85×10^{-3}	1.00×10^{-3}	3.13×10^{-3}
LM 5×5 SymAv1	5.03×10^{-4}	9.74×10^{-4}	1.40×10^{-4}	8.67×10^{-4}
LM 5×5 SymAv2	2.29×10^{-4}	2.05×10^{-4}	1.53×10^{-4}	3.06×10^{-4}
LM 7×7 Asym	1.66×10^{-2}	1.34×10^{-2}	1.16×10^{-2}	2.16×10^{-2}
LM 7×7 SymAv1	1.63×10^{-3}	1.63×10^{-3}	1.03×10^{-3}	2.24×10^{-3}
LM 7×7 SymAv2	4.28×10^{-4}	4.90×10^{-4}	2.45×10^{-4}	6.11×10^{-4}
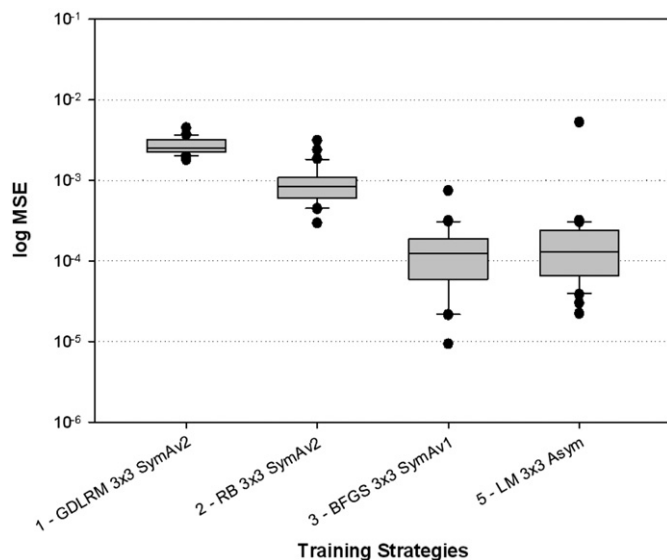
Fig. 8. The box plots of best training strategies considered for each training algorithm (GDLRM, RB, BFGS and LM).

strategies assumed for each training algorithm. Table 5 exhibits the average MSE, standard deviation and confidence interval of the mean at level 95% for the best training strategies considered.

6. Discussion

A visual analysis of the segmented images in Figs. 4b–7b gives an idea of the classification processes for the image of interest (Fig. 1), based on the classification task performed by the ANNs trained with the algorithms GDLRM 3×3 SymAv2, RB 3×3 SymAv2, BFGS 3×3 SymAv1 and LM 3×3 Asym. The visual results

Table 5
Average MSE, standard deviation on interval of confidence for the best results training strategies considered.

	Av. MSE	St. dev.	t-Int1	t-Int2
GDLRM 3×3 SymAv2	2.69×10^{-3}	6.23×10^{-4}	2.46×10^{-3}	2.92×10^{-3}
RB 3×3 SymAv2	9.82×10^{-4}	5.99×10^{-4}	7.59×10^{-4}	1.21×10^{-3}
BFGS 3×3 SymAv1	1.52×10^{-4}	1.41×10^{-4}	9.90×10^{-5}	2.04×10^{-4}
LM 3×3 Asym	3.17×10^{-4}	9.37×10^{-4}	0	6.67×10^{-4}

of the segmentation are evidence that the training strategies presented are satisfactory.

Comparing the symmetry information (Asym, SymAv1 and SymAv2) used as input, according to Tables 1–4, the symmetries SymAv1 and SymAv2 reduce the average of the MSEs (exception for LM 3×3 SymAv1) and the values of standard deviation (exceptions for GDLRM 3×3 SymAv1 and RB 5×5 SymAv2) in most of the cases, with respect to the strategy Asym. The probable reason is that, for SymAv1 and SymAv2, there was a reduction of the dimensionality of the inputs given to the ANNs and therefore the weights to be adjusted during the training phase. In addition, the intensity averaging reduced the noise of the input information presented to the ANNs.

Comparing the kernels, according to Tables 1–4, for the training algorithms GDLRM and RB, the use of the strategies 3×3 leads to lower averages than the corresponding 5×5 and 7×7 strategies (with the exception of LM 5×5 SymAv2). Broadly speaking, the best training strategies among the tested ones use a 3×3 kernel and information symmetries SymAv1 or SymAv2, and are likely to yield a lower MSE.

As many training strategies give good results, selecting a single best one for bone pixel recognition in SR X-ray μCT images is non-trivial: in Fig. 6a (algorithm BFGS) for example, we find the combinations 2 and 3 to have very similar box plots. The same happens in Fig. 7a (algorithm LM) for the combinations 1 and 3.

In an additional comparison, we found that the best combinations were GDLRM 3×3 SymAv2, RB 3×3 SymAv2, BFGS 3×3 SymAv1 and LM 3×3 Asym, whose box plots are depicted in Fig. 8. According to Table 5, it is possible to say that for all these combinations the average MSE is very low, but still lower for the best combinations of the algorithms BFGS and LM. Going back to the initial problem of recognizing bone pixels in SR X-ray μCT images, our methodology of validation now allows us to affirm that the tests were successful, in the sense that the ANNs achieve very low average MSE for the image of interest. In addition, the LOOCV methodology provides a good estimate of bias and variance for future processes of classification.

7. Conclusion

SR X-ray μCT enables magnified images which may be used as a non-invasive and non-destructive technique for diagnosis and treatment of diseases, for example, the osteoporosis which has become a major public health problem. Not only bony mass quantification is important, but recent studies point out to the fact that structural analysis is also important for such diseases. HMM provides parameters that allow the structural analysis of the bone. However, as the μCT is relatively new, there is no full agreement or standardization of methods and procedures for HMM based on μCT images, especially in the case of SR X-ray μCT images, therefore requiring further investigation. In this article, an extensive assessment of well-known architectures and training algorithms for ANNs, symmetries and kernels was performed, with an analysis of the results, as a first step in order to survey techniques for bone HMM based on SR μCT images. Several

training strategies have yielded outstanding results for the bone pixel recognition to be applied to HMM, with a satisfactory segmentation of the image of interest based on the bone pixel classification performed by the ANNs.

Acknowledgements

References

[1] F.R. Elder, A.M. Gurewitsch, R.V. Langmuir, H.C. Pollock, Phys. Rev. 71 (1947) 829.
[2] R.C. Barroso, R.T. Lopes, E.F.O. de Jesus, L.F. Oliveira, Nucl. Instr. and Meth. A 471 (2001) 75.
[3] R.T. Lopes, H.S. Rocha, E.F.O. de Jesus, R.C. Barroso, L.F. Oliveira, M.J. Anjos, D. Braz, S. Moreira, Nucl. Instr. and Meth. A 505 (2003) 604.
[4] G.N. Hounsfield, Br. J. Radiol. 46 (1973) 1016.
[5] B. Borah, G.J. Gross, T.E. Dufresne, T.S. Smith, M.D. Cockman, P.A. Chmielewski, M.W. Lundy, J.R. Hartke, E.W. Sod, Anat. Rec. 265 (2001) 101.
[6] L.A. Feldkamp, S.A. Goldstein, A.M. Parfitt, G. Jesion, M. Kleerekoper, J. Bone Miner. Res. 4 (1989) 3–11.
[7] L.D. Carbonare, M.T. Valenti, F. Bertoldo, M. Zanatta, S. Zenari, G. Realdi, V. Lo Cascio, S. Giannini, Micron 36 (2005) 609.
[8] D. Chappard, M.-F. Baslé, E. Legrand, M. Audran, Morphologie 92 (2008) 162.
[9] F.H. Glorieux, R. Travers, A. Taylor, J.R. Bowen, F. Rauch, M. Norman, A.M. Parfitt, Bone 26 (2000) 103.
[10] S.S. Budden, M.E. Gunness, Brain Dev. 23 (2001) S133.
[11] G. Dvorak, K. Reich, S. Tangl, C.A. Lill, M. Gottschalk-Baron, G. Watzek, R. Gruber, R. Haas, Arch. Oral Biol. 54 (2009) 857.
[12] C. Schouten, G.J. Meijer, J.J.J.P. van den Beucken, P.H.M. Spawen, Biomaterials 30 (2009) 4539.
[13] S. Haykin, in: Neural Networks: A Comprehensive FoundationPearson Education, India, 2005.
[14] A.A.M. Meneses, C.J.G. Pinheiro, R. Schirru, R.C. Barroso, D. Braz, L.F. Oliveira, IEEE Nucl. Sci. Symp. Med. Imaging Conf. Rec. (2008) 5309.
[15] D.E. Rumelhart, G.E. Hinton, R.J. Williams, Nature 323 (1986) 533.
[16] R. Kohavi, in: C.S. Mellish (Ed.), Proceedings of IJCAI-95Morgan Kaufmann, USA, 1995, p. 1137.
[17] F. Arfelli, et al., Radiology 215 (2000) 286.
[18] A. Olivo, Nucl. Instr. and Meth. A 548 (2005) 194.
[19] R.A. Lewis, Phys. Med. Biol. 49 (2004) 3573.
[20] A. Mamose, T. Takeda, Y. Itai, K. Hirano, Nat. Med. 2 (1996) 473.
[21] A.C. Kak, M. Slaney, in: Principles Of Computerized Tomographic ImagingIEEE Press, USA, 1988.
[22] L.F. Oliveira, R.T. Lopes, E.F.O. de Jesus, D. Braz, Nucl. Instr. and Meth. A 505 (2003) 573.
[23] L.F. Oliveira, R.T. Lopes, Nucl. Instr. and Meth. A 525 (2004) 406.
[24] A. Odgaard, Bone 20 (1997) 315.
[25] A.M. Parfitt, M.K. Drezner, F.H. Glorieux, J.A. Kanis, H. Malluche, P.J. Meunier, S.M. Ott, R.R. Recker, J. Bone Miner. Res. 2 (1987) 595.
[26] M. Egmont-Petersen, D. de Ridder, H. Handels, Pattern Recognition 35 (2002) 2279.
[27] H. Demuth, M. Beale, Neural Network Toolbox, The MathWorks, 2004.
[28] H. Sawai, IEEE Int. Conf. Neural Networks (1994) 4253.
[29] H.-S. Na, Y. Park, IEEE Int. Jt. Conf. Neural Networks (1992) 413.